Title

Evaluation of possible reactivation of undetected faults during CO 2 injection

Authors

Blanco-Martín, Laura

Jahangir, Emad

Rinaldi, Antonio P

et al.

Publication Date

2022-12-01

DOI

10.1016/j.ijggc.2022.103794

Evaluation of possible reactivation of undetected faults during CO_2 injection

Laura Blanco-Martín[a,b,*], Emad Jahangir[a], Antonio P. Rinaldi[b,c] and Jonny Rutqvist[b]

[a]*Mines Paris, Université PSL, Centre de Géosciences, 77300, Fontainebleau, France*
[b]*Lawrence Berkeley National Laboratory, Energy Geosciences Division, 94720, Berkeley, USA*
[c]*Swiss Seismological Service, Swiss Federal Institute of Technology, ETH Zürich, 8092, Zürich, Switzerland*

A B S T R A C T

Geologic storage of carbon dioxide can efficiently contribute to reduce greenhouse gas emissions to the atmosphere. Two major hazards of this technology are leakage towards the ground surface and fluid-induced seismicity. While major faults may be detected and avoided during site characterization, undetected subseismic faults could be encountered once injection has started.

This paper investigates leakage and reactivation of undetected faults through coupled thermal-hydraulic-mechanical modeling. The simulations are performed using a recently developed sequential simulator, TOUGH-Pylith, that allows to accurately account for the thermodynamics of brine-CO_2 mixtures, and to model faults as surfaces of discontinuity using state-of-the-art fault friction laws. The simulator is benchmarked against well-known analytical solutions and subsequently applied to investigate two cases of CO_2 injection close to undetected faults under normal and strike-slip faulting regimes. Although the scenarios are generic and represent unfavorable conditions, they suggest that leakage could occur and that undetected faults could trigger minor seismic events. Therefore, careful site characterization and continuous monitoring during operations should be always performed.

1. Introduction

Carbon dioxide (CO_2) emissions to the atmosphere are the main contributors to anthropogenic global warming (Collins et al., 2013). Important strategies to reduce greenhouse gas emissions include enhancing the efficiency of energy use, transitioning from fossil to low-carbon energy, and implementing carbon capture, utilization and storage (CCUS) (IEA, 2022). In CCUS, CO_2 is captured from fuel combustion and industrial processes, transported by ships or pipelines, and either used as a resource or permanently stored in deep underground formations. Here, we focus on CO_2 underground storage, for which extensive experimental, theoretical and numerical investigations have been undertaken, see *e.g.* Chu (2009); Sarkus et al. (2016); Raza et al. (2019); Cooper (2009); IEA (2008); Iglauer (2011); Ennis-King & Paterson (2001); Leung et al. (2014); Rutqvist (2012); Herzog (2016).

Potential risks associated with CO_2 sequestration must be evaluated prior to any site implementation. In addition to possible leakage (Meguerdijian & Jha, 2021), one aspect of concern is induced seismicity through the activation of faults (Pawar et al., 2015; Vilarrasa & Carrera, 2015; Zoback & Gorelick, 2012). Faults are conceptually zones of discontinuity within underground formations, and as such they often have markedly different properties compared to the surrounding layers (*e.g.,* reduced stiffness, orders-of-magnitude different permeability). In the Earth's upper

*Corresponding author
laura.blanco_martin@minesparis.psl.eu (L. Blanco-Martín)
ORCID(s): 0000-0003-1794-3227 (L. Blanco-Martín)

crust, fault zone architecture typically consists of a low-permeability core surrounded by a damaged zone having higher permeability (Caine et al., 1996; Sibson, 1977; Wibberley & Shimamoto, 2003). As the injection proceeds, the *in situ* stress state is modified in the storage formation and surrounding layers. If a fault is present, slip along the weakest surface could be triggered, with possible aseismic or seismic response. It should be noted however that to date, measured seismicity associated with CO_2 sequestration is limited to microseismicity and some minor felt events (White & Foxall, 2016): exploration and high resolution geophysical reflection surveys are conducted prior to any injection operation and help characterizing the target formations and detecting major faults. On the other hand, minor faults (often referred to as the subseismic region, *e.g.* Lohr et al. (2008)), having negligible initial offset across geological layers, could be unnoticed during site selection and characterization. Reactivation of undetected faults has been discussed in the literature. Mazzoldi et al. (2012) and Rinaldi et al. (2014) performed 2D hydro-mechanical (HM) modeling in a reservoir system intersected by a subseismic fault having no vertical offset with the aim of studying the integrity of the reservoir, possible seismicity and CO_2 leakage as a result of fault reactivation. Later, Rinaldi et al. (2015) extended the model to 3D and investigated the influence of well orientation. Using the same conceptual model, Mortezaei & Vahedifard (2015) performed 2D thermal-hydraulic-mechanical (THM) modeling to investigate the seismic potential. In this case, the thermal effect was considered by means of a heat flux, without considering the full thermodynamics of CO_2-brine mixtures. Rohmer (2014) performed 2D HM modeling to investigate the influence of dissimilar properties and thicknesses across a subseismic fault. Le Gallo (2016) performed 3D HM modeling of a potential injection site in the Paris basin to investigate CO_2 leakage and to evaluate the effect of the overpressure in the stress field. A subseismic fault extending up to a control aquifer was present not far from the injection well. In these works, the fault zone was implemented in a continuum framework, without including a surface of discontinuity. In the current work, we take a step forward and include an interface within the fault zone. Two scenarios of undetected faults, in normal and strike-slip regimes, are investigated through numerical modeling.

The underground injection of CO_2 is a multi-physics problem and involves, at least, thermal, hydraulic and mechanical coupled processes. Coupled numerical modeling of CO_2 sequestration and fault reactivation is extensive in the literature, with conceptual models, numerical approaches and material behavior covering a wide range of complexity, *e.g.* Rutqvist et al. (2002); White & Borja (2008); McClure & Horne (2011); Cappa & Rutqvist (2011); Meng (2017); Jin & Zoback (2018); Torberntsson et al. (2018); Yang & Dunham (2021); Jha & Juanes (2014); Dieterich et al. (2015); Vilarrasa et al. (2010). The fault zone can be modeled either as a continuum having different (often reduced) mechanical properties as compared to the adjacent formations (Rinaldi et al., 2014), or as a region including one or several surfaces of discontinuity that allow to model slip using advanced laws more representative of fault frictional strength (Jha & Juanes, 2014). The main advantage of the latter is that it allows for a more accurate estimation of the induced events; however, it often requires the use of specialized codes. In this work, we use two existing codes to perform sequential two-way THM coupling, TOUGH2 (Pruess et al., 2012) and Pylith (Aagaard et al., 2017, 2013), and take advantage of their strengths: TOUGH2 includes several Equation-Of-State (EOS) modules to model non-isothermal subsurface multiphase and multicomponent flow, and Pylith allows for the modeling of continua and fault surfaces, the latter being implemented as zero-thickness cohesive cells. The codes are successfully coupled for the first time in a THM framework, allowing to conduct coupled simulations accounting for the thermodynamics of the relevant fluids, and for faults in a more realistic manner.

In this paper, we first present the TOUGH-Pylith simulator and briefly describe the coupling approach and fault interface implementation. Then, the coupling is verified against analytical solutions of coupled processes. In section 4, we apply the simulator to investigate CO_2 injection into deep saline aquifers intersected by subseismic faults, with a focus on possible fault reactivation and leakage. Some conclusions and perspectives are given in the last section.

2. Material and Methods

2.1. Numerical simulator

TOUGH-Pylith is a sequential simulator for coupled THM processes modeling based on the sequential coupling of TOUGH2 (Pruess et al., 2012) and Pylith (Aagaard et al., 2017, 2013). A rich discussion of different approaches to perform coupled THM simulations (fully coupled, sequential, one-way, two-way) is available in the literature (see *e.g.* Dean et al. (2006); Kim et al. (2009)) and is out of the scope of this work. TOUGH2 allows for the modeling of multiphase, multicomponent and non-isothermal flow in porous and fractured media, and is based on the integral finite difference method. One main advantage of TOUGH2 is that it includes a wide range of EOS modules that permit to account for the thermodynamic behaviour of pure fluids and mixtures encountered in natural and anthropogenic processes in the subsurface (water, air, oil, CO_2, NaCl, hydrogen, water-NaCl-CO_2, …). In turn, Pylith allows for the computation of geomechanical equilibrium under static, quasi-static and dynamic conditions, in domains including discontinuities at different scales. This open-source, finite-element code embeds several constitutive laws for faults, and provides templates to implement additional bulk and fault models. While TOUGH2 is written in Fortran77, Pylith is written in `C++` and Python. Pylith allows for parallel computing and TOUGH2 runs in serial; however, a recent version, TOUGH3, can be run in parallel (Jung et al., 2017).

Similarly to TOUGH-FLAC (Rutqvist, 2011; Blanco-Martín et al., 2017), TOUGH-Pylith is based on the fixed-stress split sequential method to couple flow and geomechanics (Kim et al., 2009). After an initial version of the simulator (Miah et al., 2015; Miah, 2016), its full development has been achieved recently. The governing equations of the flow and geomechanics sub-problems are solved one at a time within a time step, and relevant information (pore pressure, temperature, volumetric deformation, etc.) is passed between sub-problems using the intermediate solution information technique (Settari & Mourits, 1998). Figure 1 shows a schematic representation of the coupling sequence.

In each time step, the flow sub-problem is solved first, and after convergence (circle in the Figure), relevant information is passed to the geomechanics sub-problem *via* a THM interface (arrow "1" in the Figure) to compute geomechanical equilibrium under drained conditions. Every time the coupling is made (square in the Figure), the total stress tensor is updated using

$$\underline{\underline{\sigma}}^{new} = \underline{\underline{\sigma}} - \alpha \Delta P \underline{\underline{1}} - 3\alpha_{th} K \Delta T \underline{\underline{1}} \tag{1}$$

where $\underline{\underline{\sigma}}^{new}$ is the updated total stress tensor, $\underline{\underline{\sigma}}$ is the total stress tensor at the end of the previous Pylith run, $\underline{\underline{1}}$ is the unit tensor, $K = \frac{E}{3(1-2\nu)}$ is the bulk modulus (E is the Young's modulus and ν is the Poisson's ratio), α is the Biot coefficient, α_{th} is the linear thermal expansion coefficient, and ΔP and ΔT are respectively the changes in pore pressure and temperature between two consecutive TOUGH2 time steps. Pressure, temperature and fluid mass are transferred to Pylith by means of the THM interface. Pylith then runs until mechanical equilibrium is reached (arrow "2" in the Figure). At equilibrium (triangle in the Figure), volumetric stresses (or strains) are transferred to TOUGH2 by means of the THM interface (arrow "3" in the Figure) and used to compute a mechanically-induced porosity correction in the next time step:

$$\Delta\phi = A(\alpha, \phi, K)\,\Delta P + B\left(\alpha_{th}\right)\Delta T + \Delta\phi^{corr} \tag{2}$$

where $\Delta\phi^{corr}$ is the porosity correction from geomechanics, a function of the total mean stress (Kim et al., 2012). Note that in order to compute mechanically-induced changes in other flow variables, such as permeability k or capillary pressure P_c, additional variables may be transferred through the THM interface (Rutqvist, 2011). A new time step of the flow sub-problem begins with the updated flow variables (arrow "4" in the Figure), and the described procedure is repeated until the end of the simulation.

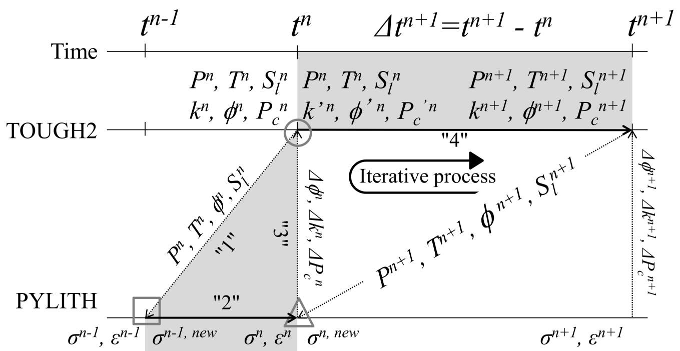

Figure 1: TOUGH-Pylith coupling sequence (adapted from Blanco-Martín et al. (2015)). The gray zones correspond to the time step marching from t^n to t^{n+1} (the symbols and labels are explained in the text).

2.2. Fault interface implementation and constitutive models

Pylith specializes in the modeling of earthquake faulting (prescribed and spontaneous ruptures) and embeds several constitutive laws for fault surfaces. However, in agreement with the classic Andersonian theory (Anderson, 1951), no distinction is made between total and effective stresses. Fault surfaces, which are not necessarily planar, are modeled using cohesive elements having no thickness and allowing in-plane and normal relative displacements (details can be found in Aagaard et al. (2017)). The fault slip vector is defined as the relative displacement between the two sides of the fault,

$$\vec{d} = \vec{u}_+ - \vec{u}_- \tag{3}$$

where $\vec{u}_+$ and $\vec{u}_-$ are the displacements on the positive and negative sides of the fault surface, respectively. Vector $\vec{d}$ has a tangent component on the fault surface, and a normal component to the fault surface. Penetration is not allowed. Likewise, the stress state in the fault is represented as a normal component, σ_n, and a shear component, τ,

$$\sigma_n = \left(\underline{\underline{\sigma}} \cdot \vec{n}\right) \cdot \vec{n} \tag{4}$$

$$\tau = \sqrt{||\underline{\underline{\sigma}}|| - {\sigma_n}^2} \tag{5}$$

where $\vec{n}$ is the fault normal vector, pointing from the negative to the positive side of the fault surface. In the context of TOUGH-Pylith, new fault constitutive models have been implemented in Pylith, in which the effective stress is used, $\underline{\underline{\sigma}}' = \underline{\underline{\sigma}} + \alpha P \underline{\underline{1}}$ (note that compression is assumed to be negative here). For such purpose, the pore pressure is passed from TOUGH2 to the fault constitutive models every time the coupling is made. In agreement with Jha & Juanes (2014), a fault pressure P_f is defined, which is a function of the pore pressure on both sides of the fault surface. Since the side on which the failure criterion is first met determines fault stability, we take $P_f = max(P_+, P_-)$ (maximum pore pressure of all adjacent cells on both sides of the fault surface). This allows to uniquely define the effective normal stress on the fault, $\sigma_n' = \left(\underline{\underline{\sigma}}' \cdot \vec{n}\right) \cdot \vec{n}$.

In order to evaluate fault stability, the shear stress on the fault is compared against a Coulomb-type criterion that provides the shear strength, τ_c,

$$\tau_c = C - \mu \cdot \sigma_n' \tag{6}$$

where C is the cohesion and μ is the friction coefficient. Note that in Pylith, if $\sigma_n' > 0$ (tensile regime), $\tau_c = C$. As long as $\tau < \tau_c$, there is no relative movement between the two sides of the fault, *i.e.*, the fault is locked. On the other hand, if the failure criterion is exceeded, slip occurs until the criterion is met again. In this case, a Lagrange multipliers approach is used. Note that when the fault surface does not reach the boundaries of the model (*i.e.,* it has buried edges), the Pylith algorithm adjusts the topology automatically, so that cohesive cells are inserted up to the buried edge, and no additional degrees of freedom are added along that edge (Aagaard et al., 2017). For this purpose, the user defines an additional group of nodes including only those that form the buried edge.

The evolution of the friction coefficient μ is described differently among the constitutive models. In this work, we focus on two models widely used to evaluate fault frictional strength: slip weakening and rate-and-state. In the slip weakening model, the coefficient of friction evolves from a peak value, μ_p, to a residual value, μ_r, as the slip $d = ||\vec{d}||$ increases from 0 to the critical slip distance, d_c:

$$\mu = \mu_p - \left(\mu_p - \mu_r\right) \frac{d}{d_c} \tag{7}$$

In the rate-and-state model, the friction coefficient evolves as a function of the slip rate, $v = ||{}^{d\vec{d}}/_{dt}||$, and also as a function of a state variable, θ:

$$\mu = \mu^* + a \ln\left(\frac{v}{v^*}\right) + b \ln\left(\frac{\theta v^*}{L}\right) \tag{8}$$

where μ^* is the friction coefficient at the reference slip rate v^*, L is the characteristic length and a, b are empirical parameters. Note that in Pylith, a linearization is applied to the friction coefficient when the slip rate falls below a threshold (Aagaard et al., 2017). The evolution of the state variable θ is given by the ageing law described in Ruina (1983),

$$\frac{d\theta}{dt} = 1 - \frac{v\theta}{L} \tag{9}$$

The state variable, homogeneous to time, represents the maturity of the asperities in the fault interface (Rice, 1993). Depending on the parameter set, this model can account both for friction increase (strengthening) and decrease (weakening). At steady-state, the state variable tends towards ${}^L/_v$ and therefore $\mu = \mu^* + (a-b)\ln({}^v/_{v^*})$. Rate-and-state allows to simulate repetitive stick-slip behavior and the seismic cycle (Dieterich, 1981). Also, as state evolution occurs over time scales in the order of ${}^L/_v$, adaptive time stepping is more efficient when using this law.

3. Verification cases

In this section, we benchmark TOUGH-Pylith against well-known analytical solutions of HM and THM coupling. Indeed, TOUGH2 and Pylith have been tested and verified previously (Aagaard et al., 2017; White et al., 2016; Pruess, 2005; Okada, 1992), but the validity of the coupling scheme between the two codes has to be demonstrated before it is applied to subsurface scenarios.

3.1. Mandel's problem (HM coupling)

Mandel's problem of poroelasticity (Mandel, 1953) is illustrated in Figure 2. A saturated porous material with rectangular cross-section and infinite length in the out-of-plane direction is sandwiched by two stiff, frictionless plates. Drainage is possible along the lateral boundaries. The sample is initially in equilibrium, and at $t = 0^+$ a compressive force is applied normal to the plates. The original resolution of this 2D plane strain problem was extended by Abousleiman et al. (1996) to account for compressible fluids and non-isotropic materials.

Initially, the load applied to the plates induces an excess of pore pressure (Skempton effect). Over time, drainage

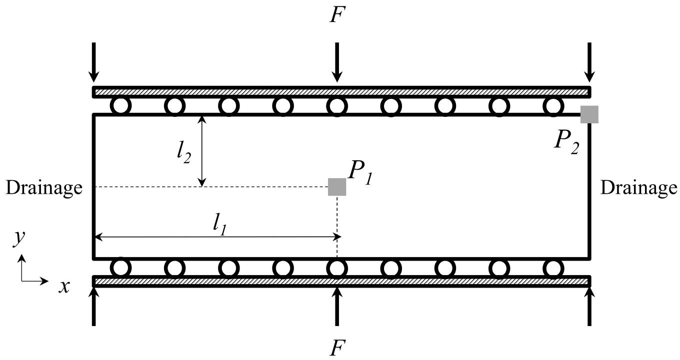

Figure 2: Schematic representation of Mandel's problem, including monitoring points P_1 and P_2 for Figure 3.

occurs at the open boundaries, which makes the laterals of the sample more compliant than its core. However, since the vertical displacement must be equal along the stiff top and bottom boundaries, there is an increase of pore pressure in the central region, yielding a non-monotonic pore pressure evolution, known as the Mandel-Cryer effect (Schiffman et al., 1969). At a later time, the excess of pore pressure dissipates completely.

For the comparison with TOUGH-Pylith, we have assumed a sample with dimensions $l_1 = 5$ m and $l_2 = 1.25$ m. Gravity is neglected and cohesive elements are inserted above and below the sample to model frictionless plates. The initial stress field is -0.1 MPa (isotropic) and at $t^+ = 0$ we apply -10 MPa normal to the plates. The initial pore pressure is 0.1 MPa. Table 1 lists the parameters used. Module EOS1 of TOUGH2 (only one component, water) is used in isothermal conditions, and we force constant viscosity, μ_f, and compressibility, C_f, for compliance with the analytical solution detailed in Abousleiman et al. (1996).

Table 1
Mandel's problem: parameters used in the simulation

Parameter (unit)	Value
k (m^2)	$6.51 \cdot 10^{-15}$
ϕ_0 (-)	0.425
E (MPa)	450
ν (-)	0
α (-)	1
μ_f (Pa $\cdot$ s)	10^{-3}
C_f (Pa^{-1})	$4.5 \cdot 10^{-10}$

Figure 3 compares the evolution of the pore pressure, relevant stresses and displacements at the monitoring points shown in Figure 2. As the plots show, the comparison is very satisfactory. Note that the differences observed initially are due to different initial states: while in the analytical solution the load is already applied and borne by the fluid, in the simulation the load is applied at $t = 0^+$.

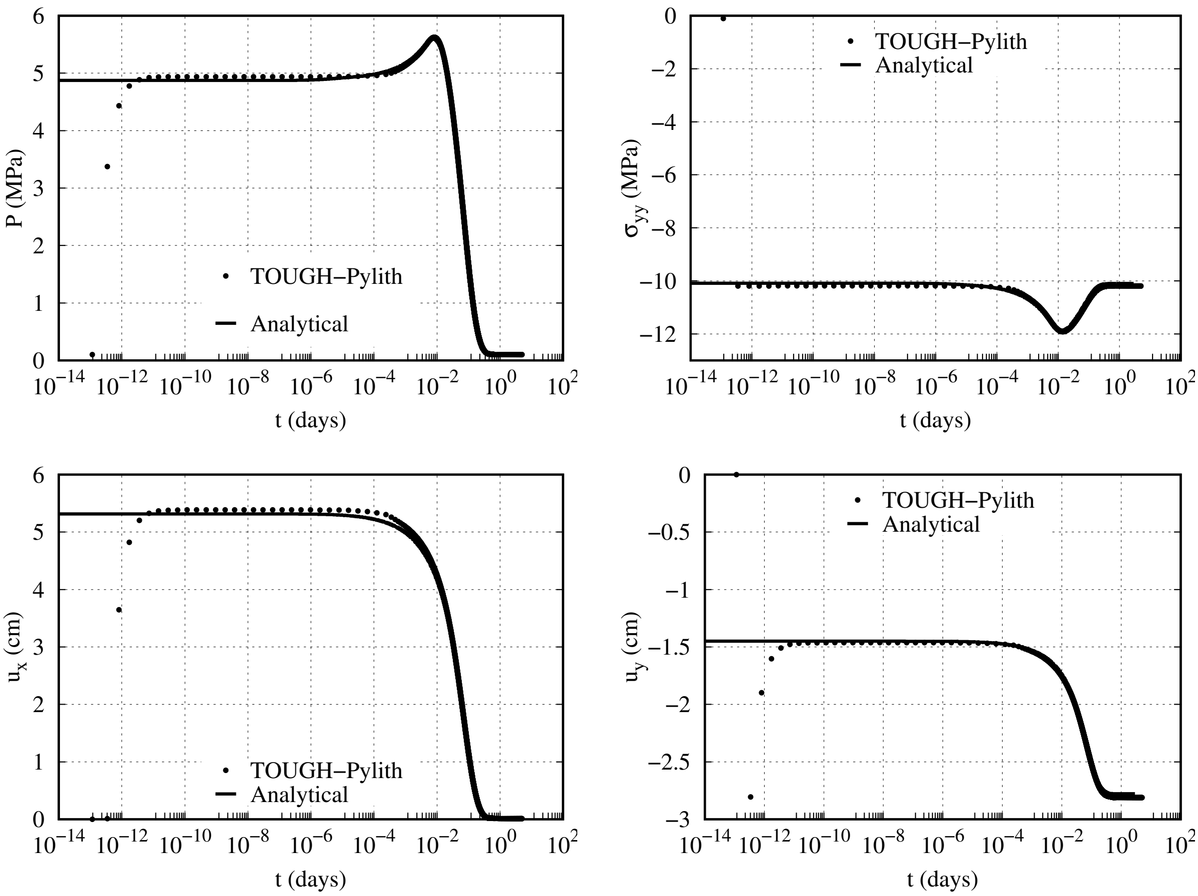

Figure 3: Mandel's problem: comparison of TOUGH-Pylith with the analytical solution in Abousleiman et al. (1996): pore pressure (upper left) and total vertical stress (upper right) at P_1, horizontal (lower left) and vertical (lower right) displacements at P_2.

Table 2
McTigue's problem: parameters used in the simulations

Parameter (unit)	Value
k (m^2)	$1.27 \cdot 10^{-19}$
ϕ_0 (-)	0.01
ρ_{gr} (kg/m^3)	2500
C (J/kg/K)	800
λ (W/m/K)	4
E (GPa)	21
ν (-)	0.25
α (-)	1
α_{th} (K^{-1})	$4 \cdot 10^{-5}$
μ_f (Pa · s)	10^{-3}
C_f (Pa^{-1})	$4.5 \cdot 10^{-10}$
α_f (K^{-1})	$1.6 \cdot 10^{-4}$

3.2. McTigue's problem (THM coupling)

McTigue (1986) proposed a theory for linear thermoporoelasticity in a saturated medium. Compressibility and thermal expansion of the fluid are taken into account. Analytical solutions for the one-dimensional heating of a half space are also provided, considering different boundary conditions for the temperature and the pressure fields. As demonstrated in the original paper, solutions for the temperature and pressure depend on the ratio of the fluid and thermal diffusivities, $R = (D_f/D_h)^{1/2}$.

Here, we investigate the case with a constant temperature boundary. Two cases are studied for the pressure field: drained and undrained boundary conditions at $x = 0$. A constant stress condition is applied normal to this boundary. A 1D model is built with sufficient extent for compliance with the analytical solution. At the boundary $x \to \infty$, the temperature, pressure and stress are kept at their initial values. Module EOS1 of TOUGH2 is used. To comply with the assumptions of the analytical solution, water viscosity (μ_f), compressibility (C_f) and expansivity (α_f) are taken as constant values. Moreover, convective heat transport is disabled, so that only conductive heat transport is active with thermal conductivity λ, and, in the heat accumulation term, grain density ρ_{gr} and specific heat C. Table 2 lists the parameters used in the simulation. The initial stress field is -0.1 MPa (isotropic), the initial pore pressure is 0.1 MPa and the initial temperature is 50 °C. At $t = 0^+$, we apply a temperature of 55 °C at $x = 0$. Figure 4 shows a schematic representation of the problem being solved and compares the simulation results with the analytical solution for different ratios of fluid and thermal diffusivities (in practice, the permeability listed in Table 2 corresponds to R_1 and a factor is applied for the cases R_2 and R_3). Overall, considering the simplifications of the analytical solution and the different definition of the pore pressure coefficient in TOUGH2 and McTigue (1986), the comparison is very satisfactory.

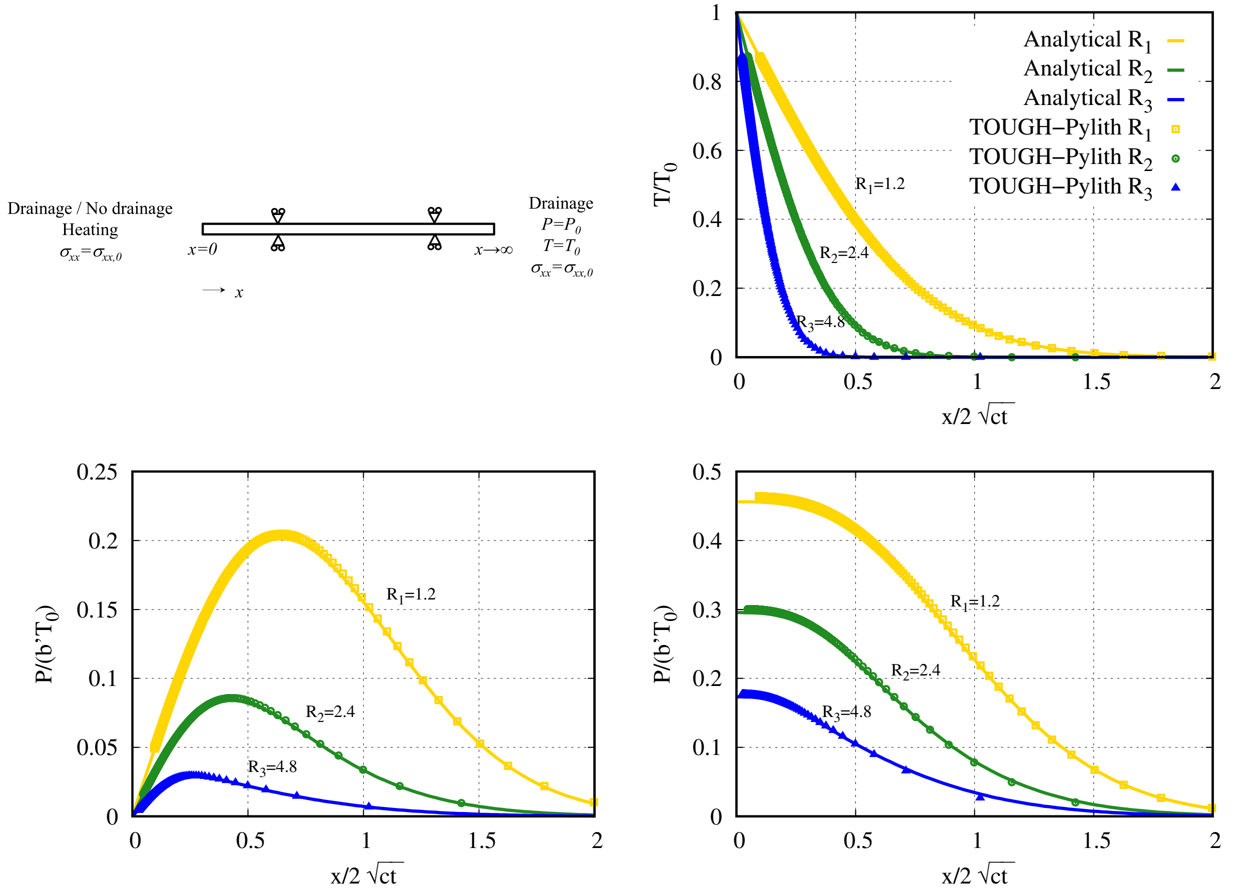

Figure 4: McTigue's problem: schematic representation (upper left) and comparison of TOUGH-Pylith with the analytical solution in McTigue (1986). Pore pressure is shown for the drained (lower left) and undrained (lower right) cases (the temperature field is the same for both, displayed in the upper right). The pore pressure coefficient b' is defined in McTigue (1986), Eq. (27).

4. CO_2 injection cases

4.1. Subseismic fault in strike-slip regime

In this section, we investigate a scenario inspired from the foreseen storage project NER300 ULCOS, which aimed to reduce CO_2 emissions related to the steel industry (Lupion & Herzog, 2013). Based on Le Gallo (2016), CO_2 injection targets lower Triassic sandstone formations, and we investigate possible leakage and induced seismicity associated with a subseismic fault, assumed to be vertical and with negligible offset. Figure 5 displays the conceptual model investigated, which considers seven material layers from the underburden (Permian basement) to the ground surface. The size of the model is $22 \times 17.5 \times 3$ km^3. The fault, which extends about 800 m along the z axis (limited vertical extent), intercepts the storage aquifer, the overlying caprock and the control aquifer. The thickness of these layers are 200, 500 and 90 m, respectively.

In the model proposed in Le Gallo (2016), the fault was oriented N155E, which is parallel to the maximum horizontal

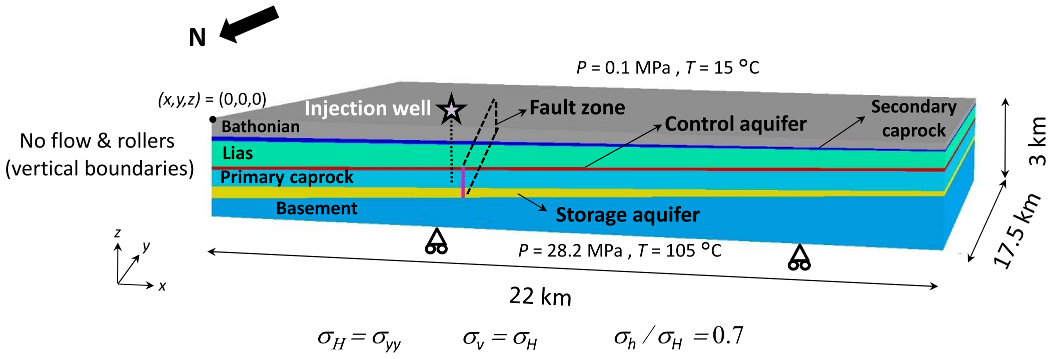

Figure 5: Subseismic fault in strike-slip regime: conceptual model.

stress (y direction in Figure 5); in these conditions, the initial shear stress on the fault is negligible and fault reactivation is highly unlikely (note that in Le Gallo (2016), the target was to investigate fault leakage rather than induced seismicity). In our scenario, the fault is oriented N145E, which corresponds to an angle of 80° between the maximum horizontal stress and the fault normal vector , or equivalently, 10° between the maximum horizontal stress and the fault direction. The thickness of the fault zone is about 100 m (x direction), and the fault core is about 20 m thick. Since field data suggest that the core-damaged zone contact may slip at an early stage during earthquakes (Cappa & Rutqvist, 2011), a fault interface is added between the fault core and the damaged zone closest to the injection well. CO_2 is injected at a depth of about 1900 m, with a rate of 0.8 Mt/y through a vertical well located about 1 km down-dip from the fault; this rate is typical of a mid-size onshore scenario. The salinity of the storage aquifer is 50 g/l. Injection conditions are $P = 25$ MPa and $T = 45$ °C (supercritical state). Table 3 lists relevant properties of the different layers and the fault; these properties are average values for each formation and are taken from the literature when available (Millien, 1993; Bésuelle et al., 2000; Vidal-Gilbert et al., 2009; Rohmer, 2014). Except for the fault interface, it is assumed that the materials behave elastically. The fault interface responds to the criterion described in Eq. (6), and the evolution of the friction coefficient follows the slip-weakening law with $C = 0$, $\mu_p = 0.2$, $\mu_r = 0.1$ and $d_c = 0.1$ m; μ_p and μ_r are purposely low to force reactivation, but could be representative of clay-rich materials that are sometimes found in the fault gouge (Ikari et al., 2011; Le Gallo, 2016). Note that the permeability of the fault core is ten times smaller than that of the damaged zone. Also, in the fault zone, the vertical permeability (k_v, along the z direction) is 40 times smaller than the horizontal permeability (k_h); this reduces possible up-dip leakage along the fault, but it is a conservative assumption for fault reactivation. Corey's relative permeability model (Pruess et al., 2012) is used for all layers with $S_{lr} = 0.1$ and $S_{gr} = 0.05$. For capillary pressure, we use van Genuchten's model (van Genuchten, 1980) with $\lambda_{VG} = 0.457$, $P_0 = 600$ kPa, $P_{cap}^{max} = 10$ MPa and $S_{lr} = 0.01$.

Regarding initial and boundary conditions, the top and bottom boundaries are kept at $P = 0.1$ MPa, $T = 15$ °C and

Table 3
Subseismic fault in strike-slip regime: parameters used in the simulation. Each layer is represented by a different color in Figure 5. For all layers, $\lambda = 2$ W/m/K, $C = 880$ J/kg/K, $\alpha_{th} = 10^{-6}$ K^{-1}, $\nu = 0.25$ and $\alpha = 1$.

Layer	ρ_{gr} (kg/m^3)	ϕ (-)	k_h (m^2)	k_v (m^2)	E (GPa)
Bathonian	2400	0.15	$5{\cdot}10^{-13}$	$5{\cdot}10^{-13}$	10
Secondary caprock	2500	0.05	10^{-15}	10^{-15}	15
Lias	2500	0.10	10^{-14}	10^{-14}	15
Control aquifer	2400	0.15	10^{-13}	10^{-13}	20
Primary caprock	2600	0.05	10^{-18}	10^{-18}	20
Storage aquifer	2400	0.15	10^{-14}	10^{-14}	20
Permian basement	2700	0.07	10^{-17}	10^{-17}	25
Fault (damaged zone)	2400	0.10	10^{-16}	$2.5{\cdot}10^{-18}$	10
Fault core	2400	0.10	10^{-17}	$2.5{\cdot}10^{-19}$	5

$P = 28.2$ MPa, $T = 105$ °C, respectively. All lateral boundaries are closed to fluid flow. For the geomechanics sub-problem, displacement is fixed to zero normal to the bottom and the lateral boundaries. Initial stress conditions are those of the Bure site (Wileveau et al., 2007). The major horizontal stress σ_H is oriented N155E, and $\sigma_H = \sigma_v$ (lithostatic). The ratio between horizontal stresses is $\sigma_h/\sigma_H = 0.7$ (Vidal-Gilbert et al., 2009). The geothermal gradient is 30 °C/km.

We use module ECO2N of TOUGH2, which accounts for the thermodynamics and thermophysical properties of H_2O-NaCl-CO_2 mixtures (Pruess, 2005). Three phases are possible: an aqueous phase, a CO_2-rich phase (liquid or gas) and solid phase (precipitated NaCl, which may reduce the effective porosity and the permeability). Phase partitioning of H_2O and CO_2 is modeled as a function of pressure, temperature and salinity using the correlations in Spycher et al. (2003); Spycher & Pruess (2005). Salting out effects (CO_2 solubility reduction with increasing salinity) are accounted for. Note that this EOS does not account for CO_2 phase changes nor mixtures of liquid and gaseous CO_2; in fact, in the scenarios that we investigate CO_2 remains in supercritical state, and phase changes do not occur. In cases where phase changes are likely, module ECO2M should be used (Pruess, 2013), with minimal impact in the coupling procedure.

Prior to the start of the injection, a simulation is run to obtain equilibrium (hydrostatic, geothermal and lithostatic gradients). Subsequently, we model 30 years of CO_2 injection, followed by a period of 20 years of post-injection phase. In the injection horizon, the initial pore pressure and temperature are about 19 MPa and 78 °C, respectively. Figure 6 shows the evolution of pore pressure in the injection area as well as in the fault. After 30 years of injection, the overpressure is about 6.5 MPa in the injection area and about 3.2 MPa in the fault area. Note that this is an unfavorable scenario, as permeability is assumed to remain constant (another assumption will be investigated in section 4.2). As the injection stops, the pore pressure decreases towards the initial value. The temperature evolution is displayed in Figure 7. As CO_2 is injected at $T = 45$ °C, the temperature decreases in the injection area, but the extent of the cooled zone does not exceed 500 m around the well. Similarly to the pressure evolution, the temperature evolves towards the initial gradient once the injection stops.

As the injection proceeds, a fraction of CO_2 is dissolved in the aqueous phase to ensure thermodynamic equilibrium

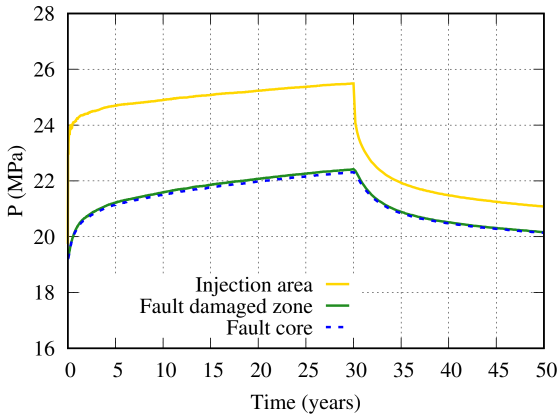

Figure 6: Subseismic fault in strike-slip regime: evolution of pore pressure in the injection and fault zones.

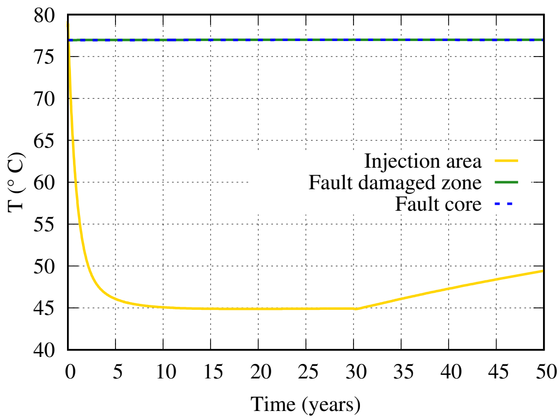

Figure 7: Subseismic fault in strike-slip regime: evolution of temperature in the injection and fault zones.

(the CO_2 concentration in the aqueous phase is about 4.5% at the given conditions). A CO_2 plume is created rapidly, and after 30 years of injection, the saturation of the CO_2-rich phase is about 65% around the well, see Figure 8. Owing to the reservoir properties and the injection rate, the CO_2 plume does not reach the fault area; therefore, in this particular scenario there is no risk of CO_2 leakage along the fault.

From a mechanical viewpoint, both the shear and the effective normal stresses on the fault plane increase, and eventually the failure criterion is reached, see Figure 9. After about 0.8 years of injection, the fault plane shows very small amounts of slip (right plot) in the upper part, which is more critically stressed as the left plot shows. After 15 years of injection, a slip event of maximum instantaneous magnitude 16 cm occurs over an area of about 2.03 km^2, affecting all the vertical extent of the fault. During this event, the friction coefficient decreases from μ_p to μ_r. Later on, there is continuous slip until the end of the injection because the failure criterion is reached due to the low value of the friction

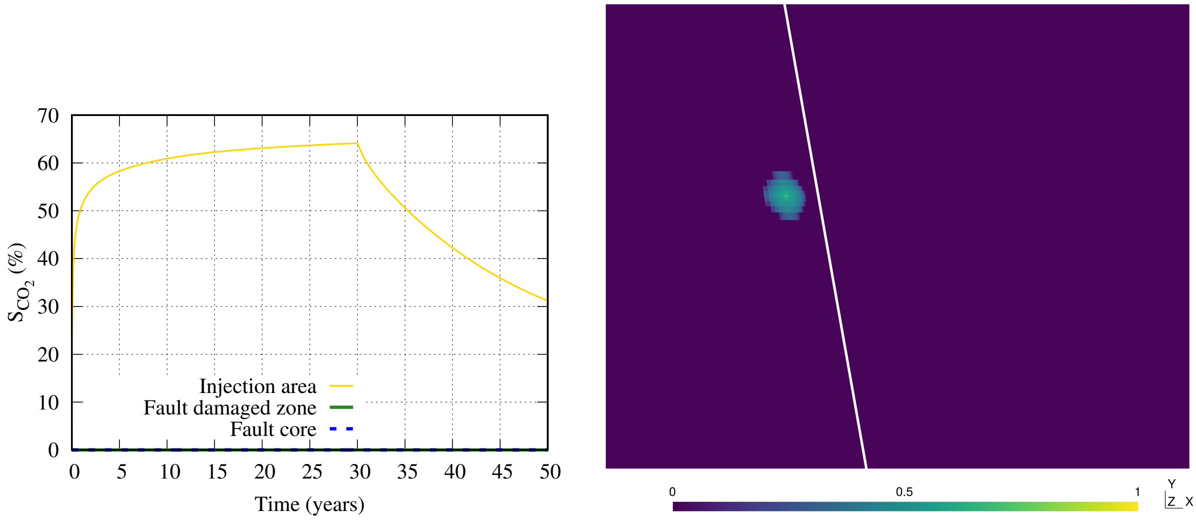

Figure 8: Subseismic fault in strike-slip regime: evolution of CO_2 plume in the injection and fault zones (left), and CO_2 plume in the storage aquifer at $t = 30$ years (the white line indicates the position of the fault) (right).

coefficient (very unfavorable conditions). Note that in this simulation we have neglected possible fault healing, so that the slip in Eq. (7) is not reset to zero every time step (accounting for fault healing may also affect the permeability evolution as discussed in Aochi et al. (2013)). Although the simulation is quasi-static, we can estimate the magnitude of the associated event at 15 years. The seismic magnitude M is calculated from the seismic moment M_0 using the following equations (Kanamori & Brodsky, 2004; Kanamori & Anderson, 1975):

$$M_0 = GAd \tag{10}$$

$$M = \frac{2}{3}\log_{10} M_0 - 6.1 \tag{11}$$

where $G = \frac{E}{2(1+\nu)}$ is the shear modulus, A is the ruptured area and d is the current slip magnitude on A (the area associated to each node is computed, and multiplied by the current slip on that node). Note that in Eq. (11), the seismic moment is expressed in N·m. Applying these equations, we get a magnitude of 3.7 at 15 years.

4.2. Subseismic fault in normal faulting regime

In this section, we investigate a scenario inspired from Rinaldi et al. (2015), in which CO_2 is injected in the vicinity of a subseismic fault. Figure 10 shows the conceptual model, with dimensions $3 \times 10 \times 2$ km^3. Owing to symmetry, the geometry shown in Figure 10 corresponds to one quarter of the total domain being modeled, which features two

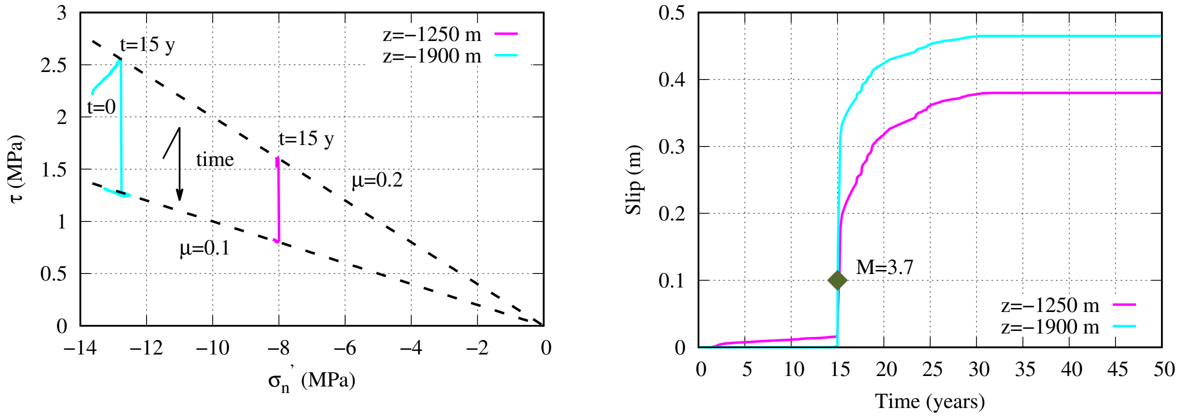

Figure 9: Subseismic fault in strike-slip regime: stress path in the storage aquifer ($z = -1900$ m) and the control aquifer ($z = -1250$ m) (left), and cumulative slip at the same locations (right). The maximum instantaneous slip at 15 years is 16 cm.

faults about 3 km apart. The storage aquifer is 100 m thick and lies between two 150 m thick caprocks. The thickness of the upper and lower aquifers is 800 m. A quasi-vertical fault (dip 80°) with negligible offset intersects the five layers shown. As in the previous case, the fault comprises a low-permeability core surrounded by a damaged zone with higher permeability. A fault interface is added between the fault core and the damage zone closest to the injection well. The thickness of the fault zone along the x axis is 90 m. CO_2 injection occurs through a vertical well located at $x \approx 1440$ m and $y = 0$, and open along the lowest 50 m of the storage aquifer layer. In this case, CO_2 is injected at a rate of 120 kg/s (3.78 Mt/y). The minimum distance between the injection well and the fault plane is 75 m; note that the high injection rate used and the well location are intended to represent an unfavorable scenario of an undetected fault that happens to be very close to the injection well, thereby increasing the likelihood of fault reactivation and leakage. Injection conditions are 15 MPa and 37 °C (supercritical state), and the salinity of the storage aquifer is 50 g/l. Table 4 lists relevant properties of the five layers and the fault. Except for the fault interface, all materials are assumed to behave elastically. Corey's relative permeability model is used for all layers with $S_{lr} = 0.3$ and $S_{gr} = 0.05$. For capillary pressure, we use van Genuchten's model with $\lambda_{VG} = 0.457$, $P_{cap}^{max} = 50$ MPa and $S_{lr} = 0$. Permeability is assumed isotropic in all layers.

In this case, the evolution of the friction coefficient follows the rate-and-state law (Eqs. (8-9)) with parameters $C = 0$, $\mu_0 = 0.6$, $v_0 = 2 \cdot 10^{-9}$ m/s, $L = 0.01$ m, $a = 0.002$ and $b = 0.08$ (note that these values favor unstable sliding). It is assumed that the fault is initially in a steady state, with $\theta = 5 \cdot 10^6$ s. To ensure stability, the maximum grid size Δx is smaller than the critical length scale, $L_c = \frac{\pi G L}{\sigma_n'(b-a)}$ (Rice, 1993). Additionally, we use adaptive time stepping.

As in Rinaldi et al. (2015), we account for mechanically-induced permeability changes along the fault. For the damaged zone, having randomly oriented fractures, we use a formulation based on experimental data on sandstone initially

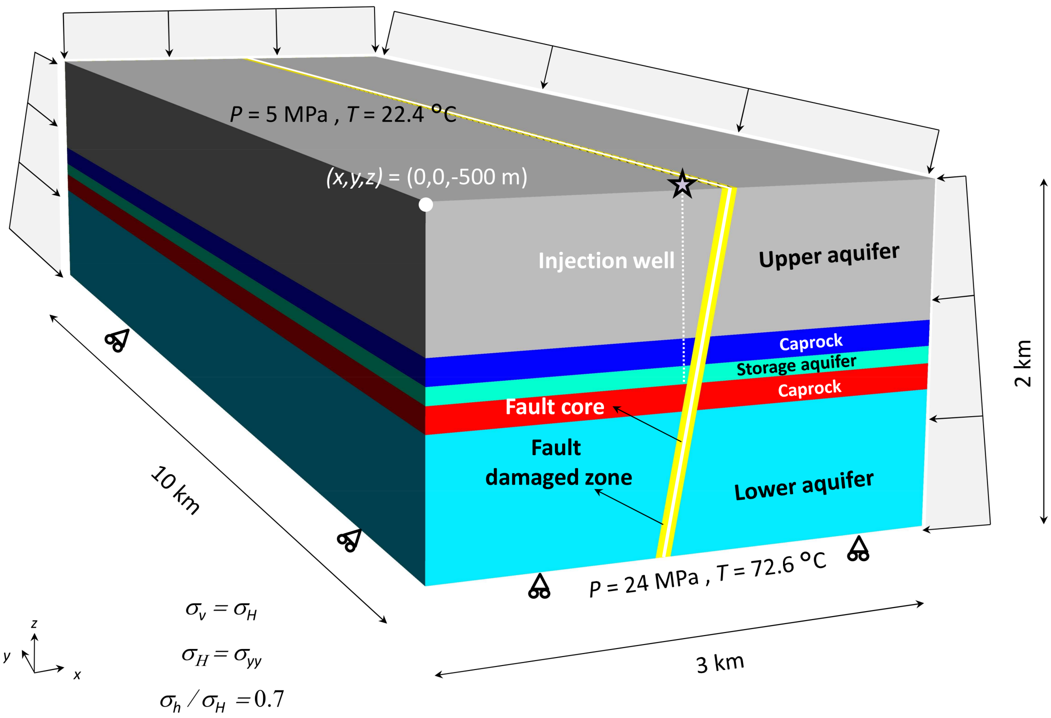

Figure 10: Subseismic fault in normal faulting regime: conceptual model.

Table 4
Subseismic fault in normal faulting regime: parameters used in the simulation. Each layer is represented by a different color in Figure 10. For all layers, $\rho_{gr} = 2260$ kg/m^3, $\phi = 0.1$, $\lambda = 1.8$ W/m/K, $C = 900$ J/kg/K, $\alpha_{th} = 10^{-5}$ K^{-1}, $\nu = 0.25$ and $\alpha = 1$.

Layer	k (m^2)	E (GPa)	P_0 (kPa)
Upper aquifer	10^{-14}	10	20
Upper caprock	10^{-19}	10	620
Storage aquifer	10^{-13}	10	20
Lower caprock	10^{-19}	10	620
Lower aquifer	10^{-18}	10	620
Fault damaged zone	$10^{-15(a)}$	10	20
Fault core	$10^{-17(a)}$	5	20

$^{(a)}$Non-constant value (see text).

proposed by Davies & Davies (2001). It relates permeability changes to changes in porosity and mean effective stress, $\Delta\sigma'_M$,

$$k_{hm} = k_0 \exp\left[22.2\left(\frac{(\phi_0 - \phi_r)\exp\left(5 \cdot 10^{-8}\Delta\sigma'_M\right) + \phi_r}{\phi_0} - 1\right)\right] \tag{12}$$

where ϕ_0 and k_0 are the initial porosity and permeability, respectively, and ϕ_r is the residual porosity, taken to be 5% (Rutqvist & Tsang, 2002). This formulation allows for up to 3 orders of magnitude change in permeability (Rinaldi et al., 2014). The fault core permeability evolves following a model inspired from Hsiung et al. (2005):

$$k_{hm} = k_0 \left[\frac{a}{1 - c\left(c\sigma'_n\right)} \sqrt{\frac{\phi_0}{12k_0}} + \frac{\phi - \phi_0}{\phi_0} \right]^3 \tag{13}$$

where

$$c = \frac{1 - \sqrt{1 + 4\sigma'_n a \sqrt{\frac{\phi_0}{12k_0}}}}{2\sigma'_{n0}} \tag{14}$$

and $a = K^{-1}$ is an empirical constant.

As for the boundary conditions, no flow is allowed across planes $x = 0$ and $y = 0$, and the displacement normal to those planes is fixed to zero. The vertical displacement is zero at $z = -2500$ m, and at $z = -500$ m, the overburden weight is applied. Pressure and temperature are fixed at the top (5 MPa, 22.4 °C) and the bottom (24 MPa, 72.6 °C) boundaries. Hydrostatic, geothermal and lithostatic gradients are applied on the lateral boundaries at $x = 3$ km and $y = 10$ km. The geothermal gradient is 25 °C/km. The minor horizontal stress is parallel to the x direction, and $\sigma_H = \sigma_v$ (lithostatic). The ratio between horizontal stresses is $\sigma_h/\sigma_H = 0.7$. Note that fault orientation relative to the stress field is intended to represent an unfavorable scenario.

Similarly to section 4.1, a first simulation is run to obtain equilibrium (hydrostatic, geothermal and lithostatic gradients). The initial pore pressure and temperature at the injection horizon are about 15 MPa and 48 °C, respectively. Subsequently, we model 5 years of CO_2 injection. Figure 11 shows the evolution of pore pressure and permeability in the injection horizon. The pressure increases rapidly with injection, and peaks at about 20 MPa after 180 days. Later on, it decreases due to the permeability increase in the fault, see right plot. This is in contrast with the pore pressure evolution in the previous scenario discussed in section 4.1, where permeability remained constant. Here, in the damaged zone permeability increases by a factor up to 300, while in the fault core, it increases up to a factor of 10. As compared to the results in Rinaldi et al. (2015), here the pressure peaks at a lower value due to the different porosity evolution model, which induces different permeability variations according to Eqs. (12-14).

The temperature evolution in the injection horizon is displayed in Figure 12. Injection of cold CO_2 reduces the temperature around the well, in an area correlated with the extent of the CO_2 plume, displayed in Figure 13. Given the high injection rate used, the proximity of the fault to the well and the fault permeability increase, leakage occurs along the fault, primarily along the damaged zone as shows the vertical profile at 5 years, and reaches the upper aquifer. Despite the permeability increase, the fault core still acts as a flow barrier, and as Figure 13 shows, no CO_2 is observed across the fault.

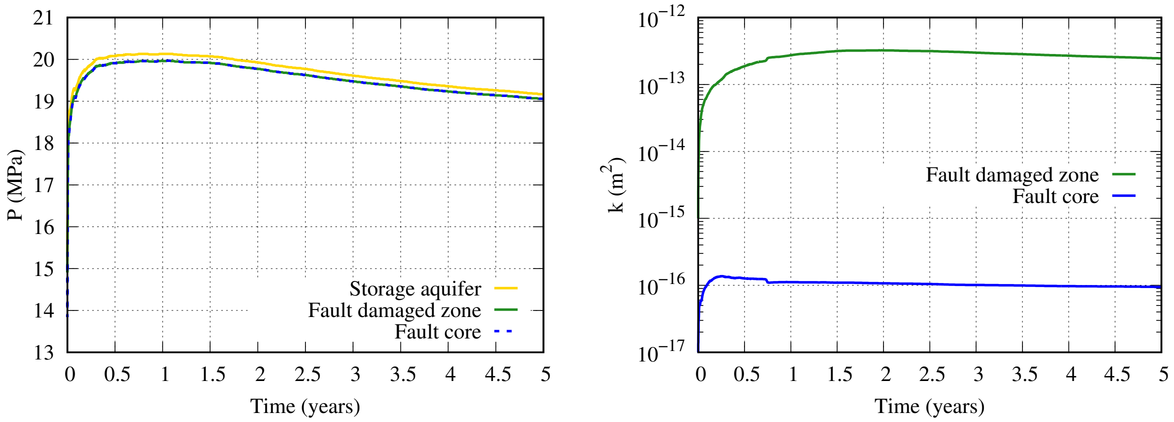

Figure 11: Subseismic fault in normal faulting regime: evolution of pore pressure in the injection horizon (left), and permeability changes in the fault core and damaged zone (right).

The stress path at different locations is displayed in Figure 14. After about 2 weeks of injection, a slip event of

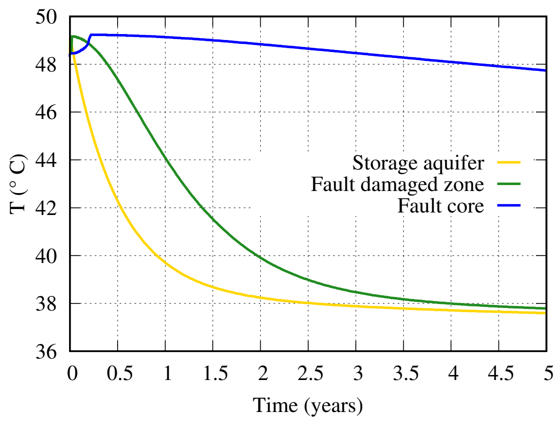

Figure 12: Subseismic fault in normal faulting regime: evolution of temperature in the injection horizon.

maximum instantaneous amplitude 6 cm occurs over an area of 94000 m^2. Using Eqs. (10-11), the associated magnitude is $M = 2.4$. Slip starts at the injection depth (bottom of storage aquifer) and propagates particularly into the underlying layers, see right plot. These evolution is consistent with previous investigations, *e.g.*,Jha & Juanes (2014); Meguerdijian & Jha (2021); Rinaldi et al. (2014). The friction coefficient decreases to 0.23 as a consequence of the reduction in the state variable during the event. Later on, it increases as the state variable increases due to slip rate reduction (Eqs. 8-9). Some minor, sudden slip events ($M \approx 1$) occur until a second $M = 2.1$ event takes place after about 270 days of injection, with an associated maximum slip of 2 cm, rupture area of 132000 m^2 and a friction coefficient reduction to 0.34. Again, after the event the friction coefficient increases as the slip rate decreases and the state variable increases. At 5 years, $\mu = 0.85$.

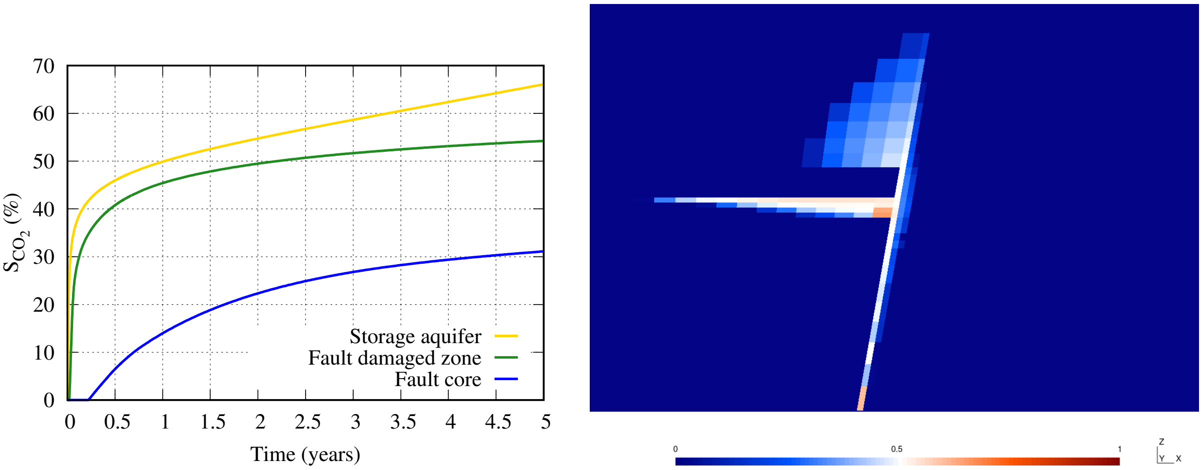

Figure 13: Subseismic fault in normal faulting regime: evolution of CO_2 plume in the injection horizon (left), and CO_2 plume at $t = 5$ years in plane y=0 (right).

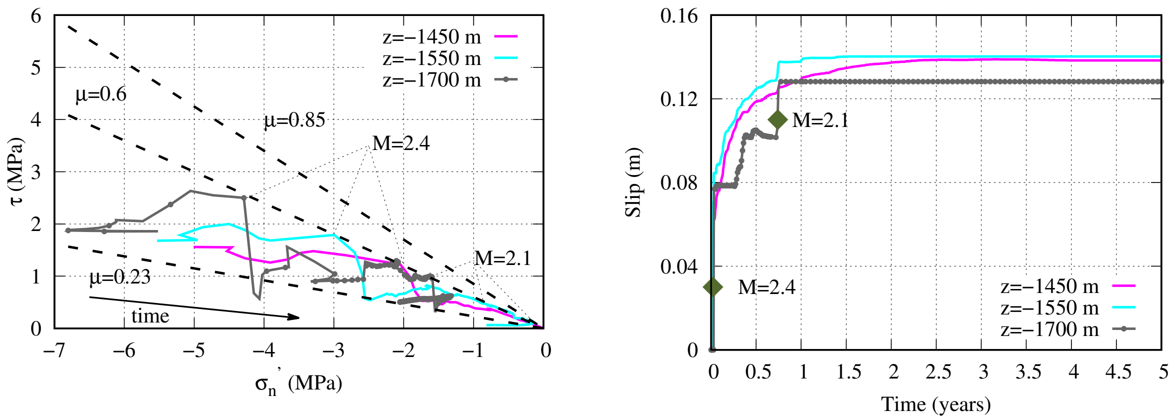

Figure 14: Subseismic fault in normal faulting regime: stress path in the storage aquifer ($z = -1450$ m, $z = -1550$ m) and the lower caprock ($z = -1700$ m) (left), and cumulative slip at the same locations (right). The maximum instantaneous slip at 14 and 270 days is 6 and 2 cm, respectively.

5. Discussion and conclusions

Geologic storage of anthropogenic CO_2 has the potential to reduce greenhouse gas emissions to the atmosphere. From the geomechanical perspective, two major hazards associated with this technology that need to be addressed before any site implementation are fault reactivation (injection-induced seismicity) and leakage along the fault. Proper site characterization conducted before injection may help detect and avoid major faults, and in fact, to date seismicity associated with CO_2 sequestration is scarce. In this paper, we focus on subseismic faults having negligible offset that could be undetected during site selection and characterization.

We perform coupled THM modeling of CO_2 injection into deep saline aquifers intersected by undetected faults under two different tectonic regimes, strike-slip and normal faulting. To study fault failure more accurately, the fault zone includes a surface of discontinuity. We perform sequential, two-way THM coupling using TOUGH-Pylith, a simulator based on the non-isothermal, multiphase and multicomponent flow simulator TOUGH2, and the geomechanics, open-source code Pylith. The two simulators are successfully coupled for the first time in a THM framework, and TOUGH-Pylith takes advantage of the strengths of the two codes, namely, a wide range of equations-of-state to account for the thermodynamic behaviour of pure fluids and mixtures, and the implementation of fault surfaces as discontinuities whose behavior is more representative of observed fault frictional strength, with quasi-static and dynamic ruptures. 2D and 3D simulations can be performed with TOUGH-Pylith. The coupling of the two codes is verified by means of comparison of numerical results with available analytical solutions. Then, we investigate two 3D cases of CO_2 injection in the vicinity of subseismic faults. The scenarios are taken from the literature and do not intend to reproduce real conditions; instead, to a certain extent they represent unfavorable situations for fault reactivation and leakage (high injection rates, moderate to high overpressures, proximity of the fault to the injection well, favorable *in situ* stress field relative to fault orientation, choice of friction parameters and permeability evolution). They suggest that minor events could be triggered, and highlight the need of thorough site characterization and careful monitoring during operations. Although not discussed here, the grid resolution used should be fine enough to accurately predict the CO_2 plume (Youssef et al., 2021) and allow for numerical stability (Rice, 1993).

In a broader sense, TOUGH-Pylith allows to investigate many situations beyond subseismic faults. For instance, it could be used to estimate leakage rates over long periods of time (Miocic et al., 2019), or to model different fault architectures (*e.g.,* homogeneous *vs.* fault system comprising a core and a damaged zone) and evaluate their impact on fault stability and possible leakage paths. In this context, the permeability evolution within the fault zone is not fully understood, and different evolution laws could be tested with the simulator, and the uncertainties could be quantified. Additionally, it could be used as a numerical support to many field studies, such as those at the decameter scale and under controlled conditions, that seek to better understand the link between induced seismicity and leakage in reservoir and caprock analogs (Guglielmi et al., 2021; Zappone et al., 2021), or the monitorability and the impacts of a fault zone on CO_2 migration (Michael et al., 2020). The applications are not solely related to CO_2 storage, but rather extend to scenarios comprising one or several faults in different natural or anthropogenic settings, such as geothermal (Amann et al., 2018) or nuclear waste disposal (Orellana et al., 2018).

Finally, it should be noted that in the cases investigated here, the fluid-induced slip rates are slow, much smaller than 0.1 mm/s, so the use of a quasi-static approach with appropriate parameters (in particular, large values of the characteristic length) is justified (Torberntsson et al., 2018). While the current methodology enables the simulation of a sudden slip, the quasi-static approach does not allow for a complete separation of aseismic and seismic slips. The resulting magnitudes could then be overestimated, as the final co-seismic deformation accounts for more than the true seismic slip. As a next stage, adapting the coupling scheme to quasi-dynamic (through the introduction of a radiation damping term in the shear stress, such as in Torberntsson et al. (2018), Yang & Dunham (2021) or Rice (1993)) and fully dynamic approaches (through the introduction of the inertial term in the momentum equation, such as in Jin & Zoback (2018) or Yang & Dunham (2021)) would extend the use of TOUGH-Pylith to investigate dynamic fault seismic slip. Additionally, the use of TOUGH3 would allow for parallelized simulations of both the flow and the geomechanics sub-problems, thereby reducing the computational time (Rinaldi et al., 2022).

Acknowledgments

Funding for this work has been provided by the French National Research Agency (ANR) through Geodenergies under contract No. 10-IEED-0810-04 (MissCO_2 project). Additional funding was provided by the U.S. Department of Energy under contract No. DE-AC0205CH11231 to the Lawrence Berkeley National Laboratory.

References

Aagaard, B. T., Knepley, M., & Williams, C. (2017). *PyLith User Manual, Version 2.2.1*. Computational Infrastructure for Geodynamics (CIG) University of California, Davis. https://geodynamics.org/resources/1673/download/pylith-2.2.1_manual.pdf.

Aagaard, B. T., Knepley, M. G., & Wiliams, C. A. (2013). A domain decomposition approach to implementing fault slip in finite-element models of quasi-static and dynamic crustal deformation. *Journal of Geophysical Research: Solid Earth*, *118*, 3059–3079. doi:10.1002/jgrb.50217.

Abousleiman, Y., Cheng, A. H.-D., Cui, L., Detournay, E., & Roegiers, J.-C. (1996). Mandel's problem revisited. *Géotechnique*, *46*, 187–195. doi:10.1680/geot.1996.46.2.187.

Amann, F., Gischig, V., Evans, K., Doetsch, J., Jalali, R., Valley, B., Krietsch, H., Dutler, N., Villiger, L., Brixel, B., Klepikova, M., Kittilä, A., Madonna, C., Wiemer, S., Saar, M. O., Loew, S., Driesner, T., Maurer, H., , & Giardini, D. (2018). The seismo-hydromechanical behavior during deep geothermal reservoir stimulations: open questions tackled in a decameter-scale in situ stimulation experiment. *Solid Earth*, *9*, 115–137. doi:10.5194/se-9-115-2018.

Anderson, E. (1951). *The Dynamics of Faulting and Dyke Formation with Applications to Britain*. New York: Oliver and Boyd.

Aochi, H., Poisson, B., Toussaint, R., Rachez, X., & Schmittbuhl, J. (2013). Self-induced seismicity due to fluid circulation along faults. *Geophysical Journal International*, *196*, 1544–1563. doi:10.1093/gji/ggt356.

Bésuelle, P., Desrues, J., & Raynaud, S. (2000). Experimental characterisation of the localisation phenomenon inside a Vosges sandstone in a triaxial cell. *International Journal of Rock Mechanics and Mining Sciences*, *37*, 1223–1237. doi:10.1016/S1365-1609(00)00057-5.

Blanco-Martín, L., Rutqvist, J., & Birkholzer, J. T. (2015). Long-term modeling of the thermal-hydraulic-mechanical response of a generic salt repository for heat-generating nuclear waste. *Engineering Geology*, *193*, 198–211. doi:10.1016/j.enggeo.2015.04.014.

Blanco-Martín, L., Rutqvist, J., & Birkholzer, J. T. (2017). Extension of TOUGH-FLAC to the finite strain framework. *Computers & Geosciences*, *108*, 64–71. doi:10.1016/j.cageo.2016.10.015.

Caine, J. S., Evans, J. P., & Forster, C. B. (1996). Fault zone architecture and permeability structure. *Geology*, *24*, 1025–1028. doi:10.1130/0091-7613(1996)024<1025:FZAAPS>2.3.CO;2.

Cappa, F., & Rutqvist, J. (2011). Modeling of coupled deformation and permeability evolution during fault reactivation induced by deep underground injection of CO_2. *International Journal of Greenhouse Gas Control*, *5*, 336–346. doi:10.1016/j.ijggc.2010.08.005.

Chu, S. (2009). Carbon capture and sequestration. *Science*, *325*. doi:10.1126/science.1181637.

Collins, M., Knutti, R., Arblaster, J., Dufresne, J.-L., Fichefet, T., Friedlingstein, P., Gao, X., Gutowski, W., Johns, T., Krinner, G., Shongwe, M., Tebaldi, C., Weaver, A., & Wehner, M. (2013). Long-term climate change: Projections, commitments and irreversibility. In *Climate Change 2013: The Physical Science Basis. Contribution of Working Group I to the Fifth Assessment Report of the Intergovernmental Panel on Climate Change* chapter 12. (pp. 1029–1136). Cambridge University Press, Cambridge, United Kingdom and New York, NY, USA.

Cooper, C. (2009). A technical basis for carbon dioxide storage. *Energy Procedia*, *1*, 1727–1733. doi:10.1016/j.egypro.2009.01.226.

Davies, J., & Davies, D. (2001). Stress-dependent permeability: Characterization and modeling. *SPE Journal*, *6*, 224–235. doi:10.2118/71750-PA.

Dean, R. H., Gai, X., Stone, C. M., & Minkoff, S. E. (2006). A comparison of techniques for coupling porous flow and geomechanics. *SPE Journal*, *11*, 132–140. doi:10.2118/79709-pa.

Dieterich, J. H. (1981). Constitutive properties of faults with simulated gouge. In *Mechanical Behavior of Crustal Rocks* (pp. 103–120). American Geophysical Union (AGU). doi:10.1029/GM024p0103.

Dieterich, J. H., Richards-Dinger, K. B., & Kroll, K. A. (2015). Modeling Injection-Induced Seismicity with the Physics-Based Earthquake Simulator RSQSim. *Seismological Research Letters*, *86*, 1102–1109. doi:10.1785/0220150057.

Ennis-King, J., & Paterson, L. (2001). Reservoir engineering issues in the geological disposal of carbon dioxide. In *Fifth international conference on greenhouse gas control technologies, Cairns* (pp. 290–295). volume 1.

van Genuchten, M. (1980). A Closed form Equation for Predicting the Hydraulic Conductivity of Unsaturated Soils. *Soil Science Society of America Journal*, *44*, 892–898. doi:10.2136/sssaj1980.03615995004400050002x.

Guglielmi, Y., Nussbaum, C., Cappa, F., De Barros, L., Rutqvist, J., & Birkholzer, J. (2021). Field-scale fault reactivation experiments by fluid injection highlight aseismic leakage in caprock analogs: Implications for CO_2 sequestration. *International Journal of Greenhouse Gas Control*, *111*, 103471. doi:10.1016/j.ijggc.2021.103471.

Herzog, H. (2016). Lessons learned from CCS demonstration and large pilot projects. *An MIT Energy Initiative Working Paper*, .

Hsiung, S., Chowdhury, A., & Nataraja, M. (2005). Numerical simulation of thermal–mechanical processes observed at the Drift-Scale Heater Test at Yucca Mountain, Nevada, USA. *International Journal of Rock Mechanics and Mining Sciences*, *42*, 652–666. doi:10.1016/j.ijrmms.2005.03.006.

IEA (2008). *CO_2 Capture and Storage: A Key Carbon Abatement Option*. doi:10.1787/9789264041417-en.

IEA (2022). https://www.iea.org/fuels-and-technologies/carbon-capture-utilisation-and-storage. Last accessed January 25, 2022.

Iglauer, S. (2011). *Dissolution trapping of carbon dioxide in reservoir formation brine - a carbon storage mechanism*. INTECH Open Access Publisher.

Ikari, M. J., Marone, C., & Saffer, D. M. (2011). On the relation between fault strength and frictional stability. *Geology*, *39*, 83–86. doi:10.1130/G31416.1.

Jha, B., & Juanes, R. (2014). Coupled multiphase flow and poromechanics: A computational model of pore pressure effects on fault slip and earthquake triggering. *Water Resources Research*, *50*, 3776–3808. doi:10.1002/2013WR015175.

Jin, L., & Zoback, M. D. (2018). Fully dynamic spontaneous rupture due to quasi-static pore pressure and poroelastic effects: An implicit nonlinear computational model of fluid-induced seismic events. *Journal of Geophysical Research: Solid Earth*, *123*, 9430–9468. doi:10.1029/2018JB015669.

Jung, Y., Pau, G. S. H., Finsterle, S., & Pollyea, R. M. (2017). TOUGH3: A new efficient version of the TOUGH suite of multiphase flow and transport simulators. *Computers & Geosciences*, *108*, 2–7. doi:10.1016/j.cageo.2016.09.009.

Kanamori, H., & Anderson, D. L. (1975). Theoretical basis of some empirical relations in seismology. *Bulletin of the Seismological Society of America*, *65*, 1073–1095.

Kanamori, H., & Brodsky, E. E. (2004). The physics of earthquakes. *Reports on Progress in Physics*, *67*, 1429–1496. doi:10.1088/0034-4885/67/8/r03.

Kim, J., Sonnenthal, E. L., & Rutqvist, J. (2012). Formulation and sequential numerical algorithms of coupled fluid/heat flow and geomechanics for multiple porosity materials. *International Journal for Numerical Methods in Engineering*, *92*, 425–456. doi:10.1002/nme.4340.

Kim, J., Tchelepi, H. A., & Juanes, R. (2009). Stability, accuracy and efficiency of sequential methods for coupled flow and geomechanics. In *SPE Reservoir Simulation Conference*. doi:10.2118/119084-MS sPE-119084-MS.

Le Gallo, Y. (2016). Hydro-mechanical influence of sub-seismic blind faults on integrity of CO_2 geological storage in deep saline aquifer. *International Journal of Greenhouse Gas Control*, *51*, 148–164. doi:10.1016/j.ijggc.2016.05.018.

Leung, D. Y., Caramanna, G., & Maroto-Valer, M. M. (2014). An overview of current status of carbon dioxide capture and storage technologies. *Renewable and Sustainable Energy Reviews*, *39*, 426–443. doi:10.1016/j.rser.2014.07.093.

Lohr, T., Krawczyk, C. M., Tanner, D. C., Samiee, R., Endres, H., Thierer, P. O., Oncken, O., Trappe, H., Bachmann, R., & Kukla, P. A. (2008). Prediction of subseismic faults and fractures: Integration of three-dimensional seismic data, three-dimensional retrodeformation, and well data on an example of deformation around an inverted fault. *AAPG Bulletin*, *92*, 473–485. doi:10.1306/11260707046.

Lupion, M., & Herzog, H. J. (2013). NER300: Lessons learnt in attempting to secure CCS projects in Europe. *International Journal of Greenhouse Gas Control*, *19*, 19–25. doi:10.1016/j.ijggc.2013.08.009.

Mandel, J. (1953). Consolidation Des Sols (étude mathématique). *Géotechnique*, *3*, 287–299. doi:10.1680/geot.1953.3.7.287.

Mazzoldi, A., Rinaldi, A. P., Borgia, A., & Rutqvist, J. (2012). Induced seismicity within geological carbon sequestration projects: Maximum earthquake magnitude and leakage potential from undetected faults. *International Journal of Greenhouse Gas Control*, *10*, 434–442. doi:10.1016/j.ijggc.2012.07.012.

McClure, M. W., & Horne, R. N. (2011). Investigation of injection-induced seismicity using a coupled fluid flow and rate/state friction model. *Geophysics*, *76*, WC181–WC198. doi:10.1190/geo2011-0064.1.

McTigue, D. F. (1986). Thermoelastic response of fluid-saturated porous rock. *Journal of Geophysical Research: Solid Earth*, *91*, 9533–9542. doi:10.1029/JB091iB09p09533.

Meguerdijian, S., & Jha, B. (2021). Quantification of fault leakage dynamics based on leakage magnitude and dip angle. *International Journal for Numerical and Analytical Methods in Geomechanics*, *45*, 2303–2320. doi:10.1002/nag.3267.

Meng, C. (2017). Benchmarking Defmod, an open source FEM code for modeling episodic fault rupture. *Computers & Geosciences*, *100*, 10–26.

Miah, M. (2016). *Development of a dynamic coupled hydro-geomechanical code and its application to induced seismicity*. Ph.D. thesis University of Mississippi.

Miah, M., Blanco-Martín, L., Foxal, W., Rutqvist, J., Rinaldi, A. P., & Mullen, C. (2015). Development of a hydro-geomechanical model to simulate coupled fluid flow and reservoir geomechanics. In *TOUGH Symposium 2015*.

Michael, K., Avijegon, A., Ricard, L., Myers, M., Tertyshnikov, K., Pevzner, R., Strand, J., Hortle, A., Stalker, L., Pervukhina, M., Harris, B., Feitz, A., Pejcic, B., Larcher, A., Rachakonda, P., Freifeld, B., Woitt, M., Langhi, L., Dance, T., Myers, J., Roberts, J., Saygin, E., White, C., & Seyyedi, M. (2020). A controlled CO_2 release experiment in a fault zone at the In-Situ Laboratory in Western Australia. *International Journal of Greenhouse Gas Control*, *99*, 103100. doi:10.1016/j.ijggc.2020.103100.

Millien, A. (1993). *Comportement anisotrope du grès des Vosges: élasto-plasticité, localisation, rupture*. Ph.D. thesis University of Grenoble I.

Miocic, J. M., Gilfillan, S. M. V., Frank, N., Schroeder-Ritzrau, A., Burnside, N. M., & Haszeldine, R. S. (2019). 420,000 year assessment of fault leakage rates shows geological carbon storage is secure. *Scientific Reports*, *9*, 769. doi:10.1038/s41598-018-36974-0.

Mortezaei, K., & Vahedifard, F. (2015). Numerical simulation of induced seismicity in carbon capture and storage projects. *Geotechnical and Geological Engineering*, *33*, 411–424.

Okada, Y. (1992). Internal deformation due to shear and tensile faults in a half-space. *Bulletin of the Seismological Society of America*, *82*, 1018–1040.

Orellana, L. F., Scuderi, M. M., Collettini, C., & Violay, M. (2018). Do scaly clays control seismicity on faulted shale rocks? *Earth and Planetary Science Letters*, *488*, 59–67. doi:10.1016/j.epsl.2018.01.027.

Pawar, R. J., Bromhal, G. S., Carey, J. W., Foxall, W., Korre, A., Ringrose, P. S., Tucker, O., Watson, M. N., & White, J. A. (2015). Recent advances in risk assessment and risk management of geologic CO_2 storage. *International Journal of Greenhouse Gas Control*, *40*, 292–311. doi:10.1016/j.ijggc.2015.06.014.

Pruess, K. (2005). *ECO2N: A TOUGH2 Fluid Property Module for Mixtures of Water, NaCl and CO_2*. Lawrence Berkeley National Laboratory University of California, Berkeley.

Pruess, K. (2013). *ECO2M: A TOUGH2 Fluid Property Module for Mixtures of Water, NaCl, and CO_2, Including Super- and Sub-Critical Conditions, and Phase Change Between Liquid and Gaseous CO_2*. Lawrence Berkeley National Laboratory University of California, Berkeley.

Pruess, K., Oldenburg, C., & Moridis, G. (2012). *TOUGH2 User's Guide, v2*. Lawrence Berkeley National Laboratory University of California, Berkeley.

Raza, A., Gholami, R., Rezaee, R., Rasouli, V., & Rabiei, M. (2019). Significant aspects of carbon capture and storage - A review. *Petroleum*, *5*, 335–340. doi:10.1016/j.petlm.2018.12.007.

Rice, J. R. (1993). Spatio-temporal complexity of slip on a fault. *Journal of Geophysical Research: Solid Earth*, *98*, 9885–9907. doi:10.1029/93JB00191.

Rinaldi, A. P., Rutqvist, J., & Cappa, F. (2014). Geomechanical effects on CO_2 leakage through fault zones during large-scale underground injection. *International Journal of Greenhouse Gas Control*, *20*, 117–131. doi:10.1016/j.ijggc.2013.11.001.

Rinaldi, A. P., Rutqvist, J., Luu, K., Blanco-Martín, L., Hu, M., Sentís, M. L., Eberle, L., & Kästli, P. (2022). TOUGH3-FLAC3D: a modeling approach for parallel computing of fluid flow and geomechanics (Preprint). *Earth and Space Science Open Archive*, (p. 36). doi:10.1002/essoar.10505967.3.

Rinaldi, A. P., Vilarrasa, V., Rutqvist, J., & Cappa, F. (2015). Fault reactivation during CO_2 sequestration: Effects of well orientation on seismicity and leakage. *Greenhouse Gases: Science and Technology*, *5*, 645–656. doi:10.1002/ghg.1511.

Rohmer, J. (2014). Induced seismicity of a normal blind undetected reservoir-bounding fault influenced by dissymmetric fractured damage zones. *Geophysical Journal International*, *197*, 636–641. doi:10.1093/gji/ggu018.

Ruina, A. (1983). Slip instability and state variable friction laws. *Journal of Geophysical Research: Solid Earth*, *88*, 10359–10370. doi:10.1029/JB088iB12p10359.

Rutqvist, J. (2011). Status of the TOUGH-FLAC simulator and recent applications related to coupled fluid flow and crustal deformations. *Computers & Geosciences*, *37*, 739–750. doi:10.1016/j.cageo.2010.08.006.

Rutqvist, J. (2012). The Geomechanics of CO_2 Storage in Deep Sedimentary Formations. *Geotechnical and Geological Engineering*, *30*, 525–551. doi:10.1007/s10706-011-9491-0.

Rutqvist, J., & Tsang, C.-F. (2002). A study of caprock hydromechanical changes associated with CO_2-injection into a brine formation. *Environmental Geology*, *42*, 296–305. doi:10.1007/s00254-001-0499-2.

Rutqvist, J., Wu, Y.-S., Tsang, C.-F., & Bodvarsson, G. (2002). A modeling approach for analysis of coupled multiphase fluid flow, heat transfer, and deformation in fractured porous rock. *International Journal of Rock Mechanics and Mining Sciences*, *39*, 429–442. doi:10.1016/S1365-1609(02)00022-9.

Sarkus, T., Tennyson, M., & Vikara, D. (2016). Geologic carbon storage. In *Fossil Fuels* chapter Chapter 3. (pp. 49–80). doi:10.1142/9789814699983_0003.

Schiffman, R. L., Chen, A. T.-F., & Jordan, J. C. (1969). An analysis of consolidation theories. *Journal of the Soil Mechanics and Foundations Division*, *95*, 285–312. doi:10.1061/JSFEAQ.0001222.

Settari, A., & Mourits, F. (1998). A coupled reservoir and geomechanical simulation system. *SPE Journal*, *3*, 219–226. doi:10.2118/50939-PA.

Sibson, R. H. (1977). Fault rocks and fault mechanisms. *Journal of the Geological Society*, *133*, 191–213. doi:10.1144/gsjgs.133.3.0191.

Spycher, N., & Pruess, K. (2005). CO_2-H_2O mixtures in the geological sequestration of CO_2. II. Partitioning in chloride brines at 12–100 C and up to 600 bar. *Geochimica et Cosmochimica Acta*, *69*, 3309 – 3320. doi:10.1016/j.gca.2005.01.015.

Spycher, N., Pruess, K., & Ennis-King, J. (2003). CO_2-H_2O mixtures in the geological sequestration of CO_2. I. Assessment and calculation of mutual solubilities from 12 to 100 C and up to 600 bar. *Geochimica et Cosmochimica Acta*, *67*, 3015 – 3031. doi:10.1016/S0016-7037(03)00273-4.

Torberntsson, K., Stiernström, V., Mattsson, K., & Dunham, E. M. (2018). A finite difference method for earthquake sequences in poroelastic solids. *Computational Geosciences*, *22*, 1351–1370. doi:10.1007/s10596-018-9757-1.

Vidal-Gilbert, S., Nauroy, J.-F., & Brosse, E. (2009). 3D geomechanical modelling for CO_2 geologic storage in the Dogger carbonates of the Paris Basin. *International Journal of Greenhouse Gas Control*, *3*, 288–299. doi:10.1016/j.ijggc.2008.10.004.

Vilarrasa, V., Bolster, D., Olivella, S., & Carrera, J. (2010). Coupled hydromechanical modeling of CO_2 sequestration in deep saline aquifers. *International Journal of Greenhouse Gas Control*, *4*, 910–919. doi:10.1016/j.ijggc.2010.06.006.

Vilarrasa, V., & Carrera, J. (2015). Geologic carbon storage is unlikely to trigger large earthquakes and reactivate faults through which CO_2 could leak. *Proceedings of the National Academy of Sciences*, *112*, 5938–5943. doi:10.1073/pnas.1413284112.

White, J. A., & Borja, R. I. (2008). Stabilized low-order finite elements for coupled solid-deformation/fluid-diffusion and their application to fault zone transients. *Computer Methods in Applied Mechanics and Engineering*, *197*, 4353–4366. doi:10.1016/j.cma.2008.05.015.

White, J. A., & Foxall, W. (2016). Assessing induced seismicity risk at CO_2 storage projects: Recent progress and remaining challenges. *International Journal of Greenhouse Gas Control*, *49*, 413–424. doi:10.1016/j.ijggc.2016.03.021.

White, M. D., Podgorney, R., Kelkar, S. M., McClure, M. W., Danko, G., Ghassemi, A., Fu, P., Bahrami, D., Barbier, C., Cheng, Q., Chiu, K.-K., Detournay, C., Elsworth, D., Fang, Y., Furtney, J. K., Gan, Q., Gao, Q., Guo, B., Hao, Y., Horne, R. N., Huang, K., Im, K., Norbeck, J., Rutqvist, J., Safari, M. R., Sesetty, V., Sonnenthal, E., Tao, Q., White, S. K., Wong, Y., & Xia, Y. (2016). *Benchmark Problems of the Geothermal Technologies Office Code Comparison Study*. Technical Report PNNL-26016 Pacific Northwest National Laboratory USA.

Wibberley, C., & Shimamoto, T. (2003). Internal structure and permeability of major strike-slip fault zones : the Median Tectonic Line in Mie Prefecture, Southwest Japan. *Journal of Structural Geology*, *25*, 59–78. doi:10.1016/S0191-8141(02)00014-7.

Wileveau, Y., Cornet, F., Desroches, J., & Blumling, P. (2007). Complete in situ stress determination in an argillite sedimentary formation. *Physics and Chemistry of the Earth, Parts A/B/C*, *32*, 866–878. doi:10.1016/j.pce.2006.03.018.

Yang, Y., & Dunham, E. M. (2021). Effect of porosity and permeability evolution on injection-induced aseismic slip. *Journal of Geophysical Research: Solid Earth*, *126*, e2020JB021258. doi:10.1029/2020JB021258.

Youssef, A. A., Tran, L., & Matthäi, S. (2021). Impact of the vertical resolution of corner-point grids on CO_2 plume migration predictions for layered aquifers. *International Journal of Greenhouse Gas Control*, *106*, 103249. doi:10.1016/j.ijggc.2021.103249.

Zappone, A., Rinaldi, A. P., Grab, M., Wenning, Q. C., Roques, C., Madonna, C., Obermann, A. C., Bernasconi, S. M., Brennwald, M. S., Kipfer, R., Soom, F., Cook, P., Guglielmi, Y., Nussbaum, C., Giardini, D., Mazzotti, M., , & Wiemer, S. (2021). Fault sealing and caprock integrity for CO_2 storage: an in situ injection experiment. *Solid Earth*, *12*, 319–343. doi:10.5194/se-12-319-2021.

Zoback, M. D., & Gorelick, S. M. (2012). Earthquake triggering and large-scale geologic storage of carbon dioxide. *Proceedings of the National Academy of Sciences*, *109*, 10164–10168. doi:10.1073/pnas.1202473109.